# Single TrAjectory Radial (STAR) Imaging

## Gordon E. Sarty*

**The number of MRI applications that use radial *k*-space data acquisition have been increasing because of their inherent robustness to motion-induced reconstruction image artifacts relative to Cartesian acquisition methods. However, images reconstructed from radial data are more prone to image degrading effects due to magnetic field inhomogeneities than images made from Cartesian data. Presented here is a method for acquiring several radial *k*-space data lines in one trajectory, the Single TrAjectory Radial, or STAR method, that is a variation of radial EPI. The STAR method allows for angular oversampling without the increase in imaging time that occurs with angularly oversampled single line imaging. It is shown that such oversampling potentially reduces the image degrading effect of magnetic field inhomogeneities so that the motion robust features of radial imaging may be realized in a segmented EPI approach.   Magn Reson Med 51:445–451, 2004. © 2004 Wiley-Liss, Inc.**

**Key words: *k*-space; reconstruction; radial acquisition; motion robustness**

Center-out *k*-space MRI has many advantages over Cartesian sampling. These advantages include localized motion artifact (1,2), especially for diffusion imaging (3,4), the reduction of flow artifact (5) and shortened minimum echo time, $T_E$. Variations on pure radial imaging have been proposed, including the use of twisting radial lines, TWIRL (6), winding hybrid interleaved radial lines, WHIRL (7), and periodically rotated overlapping parallel lines with enhanced reconstruction, PROPELLER (8). Other methods that move in, or approximately in, the radial direction include the spiral (9,10), rosette (11,12), ROSE (13), and radial EPI methods (14).

The STAR *k*-space trajectory consists of radial lines joined together at their outer radius by tangential semicircles. The radius of the joining semicircles may be lengthened to reduce the gradient slew rate requirements with the trade-off of a smaller straight line radius for the linear part of the trajectory. Samples obtained along the semicircles are therefore important for maintaining image resolution. The STAR could be used for single shot imaging in an ideal situation of a highly homogeneous main magnetic field. Interleaved STAR trajectories, however, have to be used in a practical setup.

The theory of STAR imaging is discussed in what follows, including the design of efficient *k*-space trajectories and a discussion of the gradient waveforms required to generate the trajectories. Phantom and brain imaging applications are given that demonstrate the reduction of reconstructed image artifacts through the use of increased numbers of radial acquisitions. The motion robust aspects of the STAR method are also demonstrated by imaging a subject with moving eyes.

## THEORY

STAR trajectories are built up from STAR petal building blocks. The geometry of a STAR petal is shown in Fig. 1 which shows $R$, the maximum *k*-space radius reached by the linear part of the trajectory, $r$, the radius of the circular part of the trajectory, $\alpha$, the half-angle of opening of the petal, $\theta_p$, the turning angle of the circular part, and $\mu$, the angle that the petal makes with the $k_x$ axis. From the trigonometry of the petal, it is seen that $\theta_p = \pi + 2\alpha$. Using a simple parameterization, $t$, of time that will need to be scaled to match with real time, the trajectory of a STAR petal may be described with:

$$k_x(t)$$
$$= \begin{cases} t \cos \mu, \ 0 \leq t < R \\ R \cos[\mu + \alpha]/\cos \alpha + R \tan \alpha \cos[\theta_0(\mu) + \Theta(t - R)], \\ \qquad R \leq t \leq R + t_2 \\ (2R - t + t_2)\cos[\mu + 2\alpha], \ R + t_2 < t \leq t_2 + 2R \end{cases}$$

$$[1]$$

$$k_y(t)$$
$$= \begin{cases} t \sin \mu, \ 0 \leq t < R \\ R \sin[\mu + \alpha]/\cos \alpha + R \tan \alpha \sin[\theta_0(\mu) + \Theta(t - R)], \\ \qquad R \leq t \leq R + t_2 \\ (2R - t + t_2)\sin[\mu + 2\alpha], \ R + t_2 < t \leq t_2 + 2R \end{cases}$$

where $\Theta$ is a parameter that may be used to adjust the *k*-space velocity along the circular part, $t_2 = \theta_p/\Theta$, and $\theta_0(\mu) = (3\pi/2) + \mu$. To have the data sample points spaced around the circular part with the same spacing as on the linear part, set $\Theta = 1/r = 1/(R \tan \alpha)$. It is shown below that this selection of $\Theta$ gives the maximum performance possible with a given maximum gradient amplitude.

A complete STAR *k*-space pattern may be built up by positioning a second STAR petal such that one linear trajectory from each petal lies on the same line. With the proper selection of the half-opening angle $\alpha$, a finite number of petals may be added together in this fashion to form a complete STAR pattern. If it is desired to play out a STAR pattern with $P$ equally spaced petals in $Q$ rotations (so that the radial lines sweep out $Q$ rotations over the course of the trajectory), then the angle $\alpha$ is set by:

$$\alpha = Q\pi/2P, \qquad [2]$$

Department of Psychology, University of Saskatchewan, Saskatoon, Saskatchewan, Canada.

*Correspondence to: Gordon E. Sarty, Department of Psychology, 9 Campus Drive, Saskatoon, Saskatchewan S7N 5A5, Canada. E-mail: gordon.sarty@usask.ca
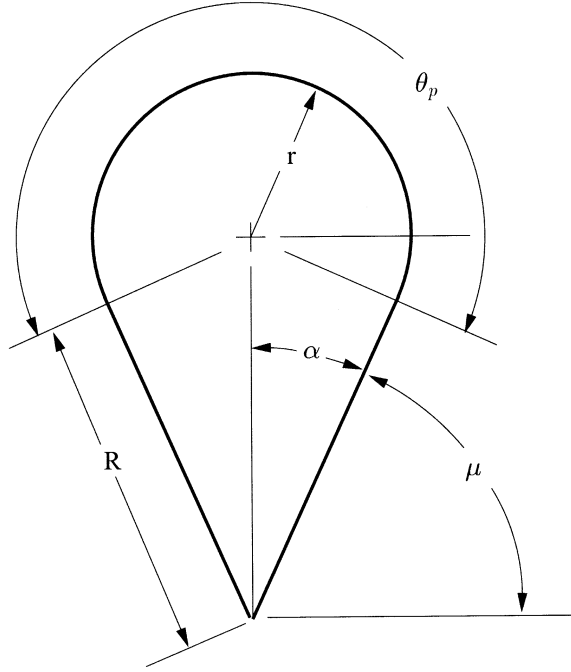
FIG. 1. The geometry of a STAR petal. The shape of the petal is defined by the parameters $R$, the length of the straight path, and $\alpha$, the half-opening angle of the petal. The petal makes an angle $\mu$ with the $k_x$ axis and the angle $\theta_p$ is the total turning angle of the circular part of the petal.

with the restriction that $\alpha \leq \pi/2$. When $\alpha = \pi/2$, $R = 0$ in Eq. [1] so that the STAR petal is reduced to a circle and $P = 1$ or 2 may be chosen. When $P > 2$, it is necessary to choose $P$ odd to obtain a continuously differentiable trajectory; one in which every petal may be reached by following the inward trajectory of one petal along the same line to the outward trajectory of the next petal. For example, to illustrate the source of Eq. [2], five petals may be distributed about 360° (one rotation), in which case $\alpha = 360°/20 = 18°$, or five petals may be distributed about 1080° (three rotations), in which case $\alpha = 1080°/20 = 54°$.

The complete STAR pattern may be described with $P$ piecewise expressions of the form given by Eq. [1] with $\mu$ replaced by $\mu_p$ for $1 \leq p \leq P$ where $\mu_p = \mu_{p-1} + 2\alpha + \pi$ for $p > 1$. The orientation of the pattern is set with the selection of $\mu_1 \equiv \mu$. To interleave the STAR patterns through rotation by an angle $\beta$, further replace $\mu$ in Eq. [1] with $\mu_p + \beta$ so that the $p^{\text{th}}$ petal of interleaf $\beta$ is described by:

$$k_{x,p}(t, \beta)$$

$$= \begin{cases} t_1(p)\cos(\mu_p + \beta), (p-1)(2R + t_2) \leq t \\ \quad < (2p-1)R + (p-1)t_2 \\ R\cos[\mu_p + \beta + \alpha]/\cos \alpha + R \tan \alpha \cos[\theta_0(\mu_p + \beta) \\ \quad + \Theta(t_1(p) - R)],(2p-1)R + (p-1)t_2 \leq t \\ \quad \leq (2p-1)R + pt_2 \\ (2R - t_1(p) + t_2)\cos[\mu_p + \beta + 2\alpha],(2p-1)R \\ \quad + pt_2 < t \leq p(2R + t_2) \end{cases},$$

[3]

$$k_{y,p}(t, \beta)$$

$$= \begin{cases} t_1(p)\sin(\mu_p + \beta), (p-1)(2R + t_2) \leq t \\ \quad \leq (2p-1)R + (p-1)t_2 \\ R\sin[\mu_p + \beta + \alpha]/\cos \alpha + R \tan \alpha \sin[\theta_0(\mu_p + \beta) \\ \quad + \Theta(t_1(p) - R)], (2p-1)R + (p-1)t_2 \leq t \\ \quad \leq (2p-1)R + pt_2 \\ (2R - t_1(p) + t_2)\sin[\mu_p + \beta + 2\alpha], (2p-1)R \\ \quad + pt_2 < t \leq p(2R + t_2). \end{cases},$$

where $t_1(p) = t - (p-1)(2R + t_2)$. The magnetic field gradients required to generate a STAR trajectory are obtained by multiplying the time derivative of Eq. [3] by $2\pi/\gamma$:

$$G_{x,p}(t,\beta)$$

$$= \frac{2\pi}{\gamma} \begin{cases} \cos(\mu_p + \beta),(p-1)(2R + t_2) \leq t < (2p-1) \\ \quad R + (p-1)t_2 \\ \Theta R \tan \alpha \cos[\mu_p + \beta + \Theta(t_1(p) - R)], \\ \quad (2p-1)R + (p-1)t_2 \leq t \\ \quad \leq (2p-1)R + pt_2 \\ - \cos[\mu_p + \beta + 2\alpha], (2p-1)R + pt_2 < t \\ \quad \leq p(2R + t_2) \end{cases}, \quad [4]$$

$$G_{y,p}(t,\beta)$$

$$= \frac{2\pi}{\gamma} \begin{cases} \sin(\mu_p + \beta),(p-1)(2R + t_2) \leq t < (2p-1) \\ \quad R + (p-1)t_2 \\ \Theta R \tan \alpha \sin[\mu_p + \beta + \Theta(t_1(p) - R)], (2p-1) \\ \quad R + (p-1)t_2 \leq t \leq (2p-1)R + pt_2 \\ - \sin[\mu_p + \beta + 2\alpha], (2p-1)R + pt_2 < t \\ \quad \leq p(2R + t_2). \end{cases}.$$

Equation [3] may be used directly for reconstruction since it is straightforward to assign a time $t$, in the given parameterization, to each data sample. Similarly, a time $t$ with $0 \leq t \leq P(2R + t_2)$ may be assigned to each point that defines the gradient pulse shape in the pulse sequence and Eq. [4], after multiplication by a suitable factor, may be used to define the gradient waveform. The multiplication factor is obtained by noting that the signal acquisition occurs in $T$ sec, which corresponds to a parameter time of $P(2R + t_2)$. So Eq. [4] must be multiplied by $P(2R + t_2)/T$ to obtain the correct gradient amplitude. The maximum gradient amplitude required for the execution of a STAR trajectory is therefore:

$$G_{\max} = \max\left(\frac{2\pi P(2R + t_2)}{\gamma T}, \frac{2\pi \Theta P(2R^2 + t_2 R)\tan \alpha}{\gamma T}\right), \quad [5]$$

where the first term gives the maximum gradient along the straight part and the second term gives the maximum gradient along the circular part of the trajectory. Selecting $\Theta = 1/R \tan \alpha$ will limit the maximum gradient seen in the circular part of the trajectory to be equal to the maximum gradient seen in the linear part. So this selection of $\Theta$ will give the fastest trajectory possible with a given gradient strength limitation.

The maximum $k$-space radius $A$ required for pixel size resolution for an $N \times N$ image with a field of view of $V$ meters is $A = N/(2V)$ (15). Referring to Fig. 1, it is clear that $A = r + (R/\cos\alpha) = R(1 + \sin \alpha)/\cos \alpha$ so that:

Table 1
STAR Sequences Implemented

| Sequence name | $\alpha$ (degrees) | $P$ | $Q$ | $B$ | $G_{max}$[a] (mT/m) | $\dot{G}_{max}$[a] (mT/m/ms) | $s_{bw}$[a,b] (kHz) | Total lines[c] |
|---|---|---|---|---|---|---|---|---|
| s1705 | 18 | 5 | 1 | 17 | 3.56 | 8.62 | 30.39 | 170 |
| s1707 | 12.86 | 7 | 1 | 17 | 4.70 | 19.84 | 40.14 | 238 |
| s3103 | 30 | 3 | 1 | 31 | 2.46 | 2.75 | 21.00 | 186 |
| s3105 | 18 | 5 | 1 | 31 | 3.56 | 8.62 | 30.39 | 310 |
| s3305 | 18 | 5 | 1 | 33 | 3.56 | 8.62 | 30.39 | 330 |
| s3305B | 54 | 5 | 3 | 33 | 5.50 | 4.34 | 46.86 | 330 |
| s6705 | 18 | 5 | 1 | 67 | 3.56 | 8.62 | 30.39 | 670 |

[a]For a field of view, *V,* equal 250 mm.
[b]The receiver bandwidth, $r_{bw}$: was 100 kHz for all sequences.
[c]Nyquist angular criterion is 402 lines.

$$R = \frac{A \cos \alpha}{(1 + \sin \alpha)} \text{ cycles/meter.} \qquad [6]$$

The gradient slew rate required for the STAR trajectory is obtained by multiplying the derivative of Eq. [4] by $P^2(2R + t_2)^2/T^2$. The maximum slew rate is therefore

$$\left. \frac{dG}{dt} \right|_{max} = \frac{2\pi P^2(2R^2 + Rt_2)^2\Theta^2\tan \alpha}{\gamma T^2}. \qquad [7]$$

The imaging data $S(t, \beta)$ may be reconstructed from a suitable approximation of the integral operator P given by

$$P\rho(x,y)$$

$$= \left| \int_0^{2\pi} \int_0^{P(2R^2+Rt_2)} S(t,\beta) e^{2\pi i(xk_x(t,\beta)+yk_y(t,\beta))} |J(t,\beta)| dt \ d\beta \right|, \quad [8]$$

where $k_x(t, \beta)$ and $k_y(t,\beta)$ are given by Eq. [3] and $|J|$ is the Jacobian determinant of the local diffeomorphism between the natural $k$-plane coordinates $(t, \beta)$ and the Cartesian coordinates $(k_x, k_y)$ (16). The Jacobian determinant is given by:

$$|J_p(t,\beta)| = \begin{cases} t - (p-1)(2R + t_2), \ (p-1)(2R + t_2) \le t \\ \quad < (2p-1)R + (p-1)t_2 \\ |\Theta R^2\cos[\alpha + \Theta R - \Theta(t - (p-1)(2R + t_2))]|, \\ \quad (2p-1)R + (p-1)t_2 \le t \le (2p-1)R + pt_2 \\ t - p(2R + t_2), \ (2p-1)R + pt_2 < t \\ \quad \le p(2R + t_2). \end{cases}$$

$$[9]$$

The required Nyquist sampling density may be estimated by applying the rules for polar sampling. That is, the spacing along the linear part of the trajectory, in the radial direction, should be such that $\Delta k = 1/V$ and the total number of petals $BP,$ which is equal to the total number of azimuthal views, should be such that $BP \ge (\pi/2)(N)$ for an $N \times N$ image reconstruction where $B$ is the number of interleaves. It is necessary that the number of interleaves $B$ be odd if it is required that no retracing of radial lines is desired.

The signal bandwidth required is:

$$S_{bw} = G_{max}V\gamma/2\pi \text{ cycles/second,} \qquad [10]$$

where $G_{max}$ is given by Eq. [5]. The receiver bandwidth is usually fixed at $r_{bw} = 1/\Delta t$ cycles/second where $\Delta t$ is the sampling dwell time. Care must be taken in the design of STAR trajectories that $s_{bw} < r_{bw}$.

## MATERIALS AND METHODS

Seven STAR sequences, with parameters as given in Table 1, were implemented on a Siemens (Erlangen, Germany) Symphony 1.5T nuclear magnetic resonance imager. The corresponding $k$-space trajectories are shown in Fig. 2. The imager was equipped with Numaris 3.5 software. The acquisition time for a single STAR trajectory was $T = 20.5$ ms with 4100 complex samples acquired in that time for all sequences. Data were acquired out to a $k$-space radius, $A$, of 256 cycles/meter for a field of view, $V$, of 250 mm. The Numaris software fixed the receiver bandwidth at 100 kHz for the sequences, a value which is half of $1/\Delta t$ because the software always assumes 2 times oversampling. A gradient echo sequence with an RF excitation flip angle of 20°, $T_R = 100$ ms, $T_E = 10$ ms was used. The transverse magnetization was not spoiled between interleaves. The proprietary built-in automatic "MAP" shim sequence was run before every image acquisition. The acquired data were reconstructed into $128 \times 128$ pixel images off-line using the GFFT (17) approximation to Eq. [8].

Sequence pairs s1705 and s1707, and s3103 and s3105 were implemented to compare the effect of increasing the angular sampling rate by increasing the number of petals, $P,$ in the individual STAR trajectories while keeping the number of interleaves, $B,$ fixed. In the former case, five leaf STAR trajectories were compared to seven leaf STAR trajectories for 17 interleaves; in the latter case three leaf STAR trajectories were compared to five leaf STAR trajectories for 31 interleaves. Sequence pair s1705 and s6705 allowed the comparison of the effect of increasing the number of interleaves while keeping the number of STAR petals fixed. To achieve strict Nyquist sampling rates in the angular direction, a total of 402 radial lines is required. The total number of radial lines provided by each sequence is given in Table 1. Of all the sequences implemented, only s6705 exceeds the strict Nyquist criterion.
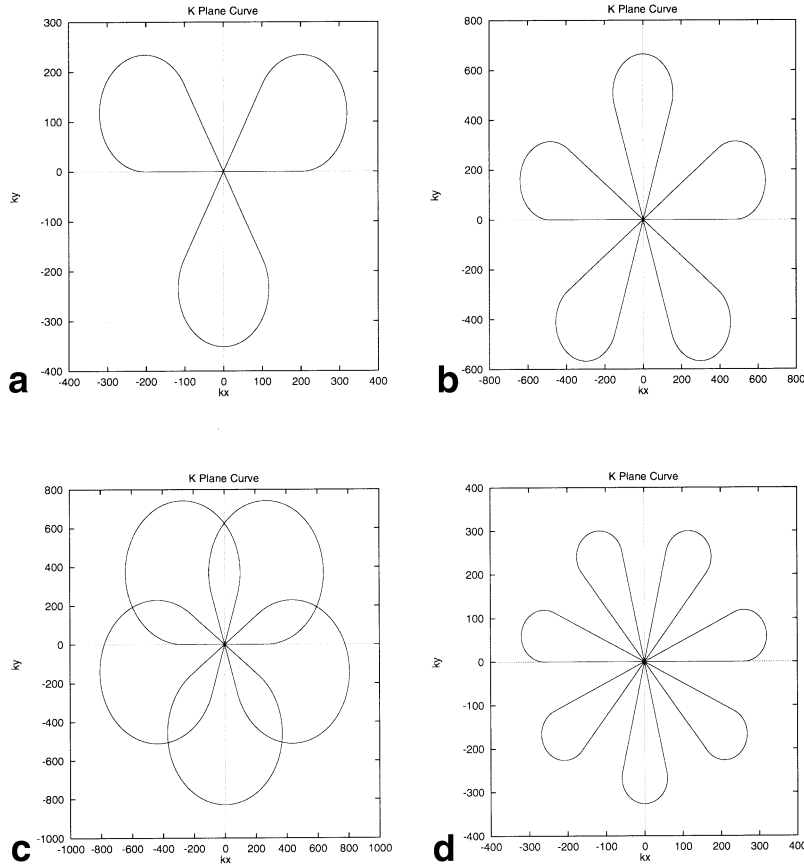
FIG. 2. STAR trajectories implemented. See Table 1 for details. **(a)** s3103, **(b)** s1705, s3105, s3305, s6705, **(c)** s3305B, **(d)** s1707. The patterns shown here are scaled for a 200 mm field of view.

However, none of the *k*-space sampling patterns used give rise to any substantial artifacts in images reconstructed from ideal simulated data (17).

Three subjects were imaged using all of the sequences listed in Table 1. A standard quality control phantom with a sharp liquid boundary and an air bubble at the top surface was imaged to investigate the effect of magnetic field inhomogeneities associated with susceptibility gradients in a typical imaged object. A 4 mm slice through a still volunteer's live brain was acquired to investigate the effect of magnetic field inhomogeneities associated with the brain and to investigate the image contrast provided by the various STAR sequences. Finally, a 4 mm slice though the eyeballs of a volunteer was imaged while the volunteer was rolling his eyeballs for the purpose of evaluating the resulting motion artifacts in the reconstructed image.

To investigate the effect of the MAP shim, the quality control phantom was imaged without and with the MAP ship applied using the built in "scout" sequence (spin warp, $T_R = 21$ ms, $T_E = 6$ ms, 300 mm × 300 mm field of view). Additionally a 200 mm spherical phantom was imaged with the s1705 and s1707 sequences twice: once with gradient values appropriate for $V = 250$ mm and once with the gradients at half the $V = 250$ mm value (see Table 1).

## RESULTS

The images acquired with sequences s1705, s1707, and s6705 are shown in Fig. 3. These images show the effect of increasing the number of STAR petals while keeping the number of interleaves fixed and the effect of increasing the number of interleaves while keeping the number of petals fixed. Increasing the number of petals in the STAR pattern while keeping the number of interleaves fixed (s1705 vs. s1707) reduced the image degrading effect of magnetic field inhomogeneities without changing the image contrast, which could be described as "$T_2$-weighted." A second comparison (s3103 vs. s3105) led to similar results but with less "$T_2$ weighting" in the $B = 31$ sequences as compared to the $B = 17$ sequences. Increasing the number of interleaves while keeping the number of petals fixed (s1705 vs. s6705) reduced the image degrading effect of magnetic field inhomogeneities and resulted in a change in image contrast. The $B = 67$ sequence had less "$T_2$ weighting" than the $B = 31$ sequences.

The results of varying the STAR petal opening angle, α, while keeping the other sequence parameters fixed, is shown in Fig. 4, where sequences s3305 and s3305B are compared. Increasing α increased the susceptibility of the sequence to image degrading artifacts.

None of the images (Figs. 3 and 4) of the subject rolling his eyeballs showed any image artifacts due to the motion. Spin warp images of the same rolling eyeball situation produced the expected image scrambling in the phase encoding direction away from the moving eyes.

All of the images in Figs. 3 and 4 show some amount of "cupping" artifact. That is, where the brightness of the image should be constant across the object it is, instead, brighter near the center. The images of the quality control

FIG. 3. The apparent sensitivity of STAR imaging to magnetic field inhomogeneities decreases as angular sampling is increased. As the sensitivity to inhomogeneities decreases, the ability to resist motion artifact increases. Shown here are images of a quality control phantom, a stationary brain slice, and a brain slice imaged at the plane of the eyeballs while the subject was rolling his eyeballs. **(a–c)** Images made with the s1705 sequence. **(d–f)** Images made with the s1707 sequence where the angular sampling was increased by increasing the number of petals *P*. Similar improvements were seen between sequences s3103 and s3105. **(g–i)** Images made with s6705 sequence where the angular sampling was increased by increasing the number of interleaves *B*.
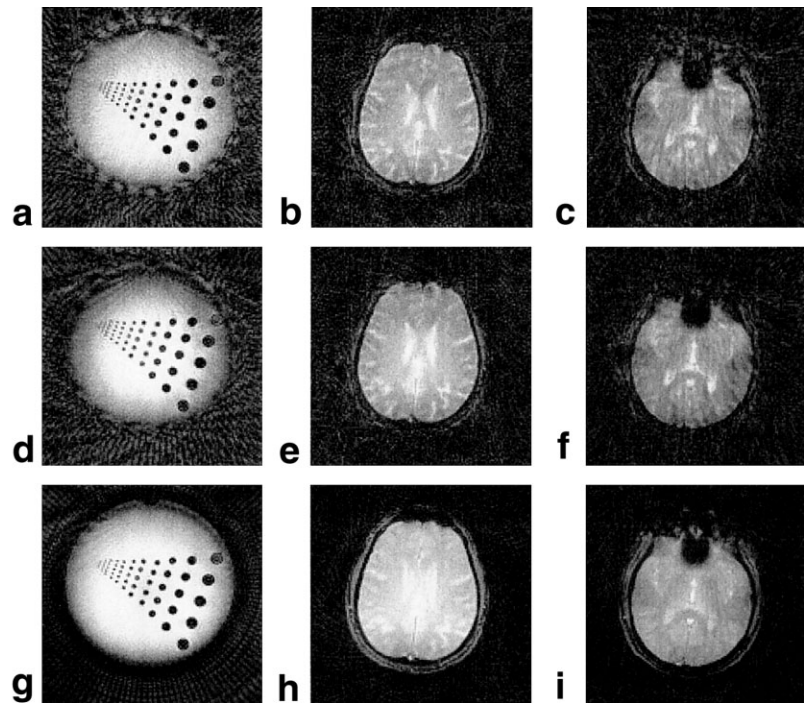
phantom taken with the scout spin warp sequence show the same cupping if the MAP shim sequence is not run prior to image data acquisition (Fig. 5a,b).

The images of the spherical phantom taken with the s1705 and s1707 sequences show two effects. One is that the severe cupping, or vignetting, is reduced, at the cost of image resolution, by reducing the gradient amplitude. The other effect is that the streak artifacts clearly emanate from the air bubble at the top of the phantom, where there is a sharp susceptibility gradient.

## DISCUSSION

Previous results by Silva et al. (14) indicated that radial EPI could be a useful alternative to Cartesian EPI for single shot imaging. The results given here indicate that such an application of rEPI is problematic, at least until automatic

shimming algorithms that are superior to the Numaris 3.5 "MAP" algorithm are used. The problem of radial imaging as compared to Cartesian imaging has always been its sensitivity to magnetic field inhomogeneities. Advances in magnet manufacturing and shimming technology have made spin warp style radial imaging possible and useful for applications such as cardiac imaging (18). It has been shown here that commercially available magnet and automatic shimming algorithms can support STAR imaging, which is essentially an interleaved version of rEPI, provided that the angular sampling is dense enough. STAR imaging may therefore offer a way of improving the spatial and/or temporal resolution of current spin warp style radial imaging methods once the apparent problems with field inhomogeneities are resolved.

The images of Fig. 5 suggest that the two main artifacts in the reconstructed STAR images, cupping and streaking,
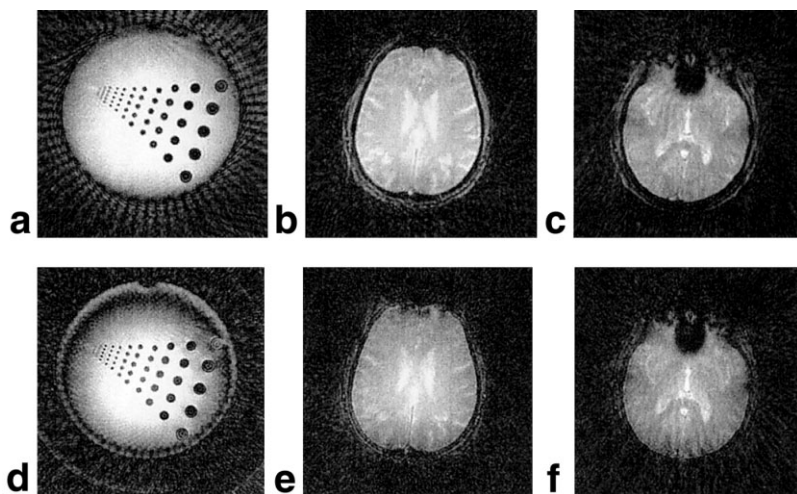


FIG. 4. Straighter STAR sequences (those with smaller α) show less reconstruction artifacts due, apparently, to magnetic field inhomogeneities. Shown here are images of a quality control phantom, a stationary brain slice, and a brain slice imaged at the plane of the eyeballs while the subject was rolling his eyeballs. **(a–c)** Images made with the narrow leaf s3305 sequence. **(d–f)** Images made with the wide leaf s3305B sequence.
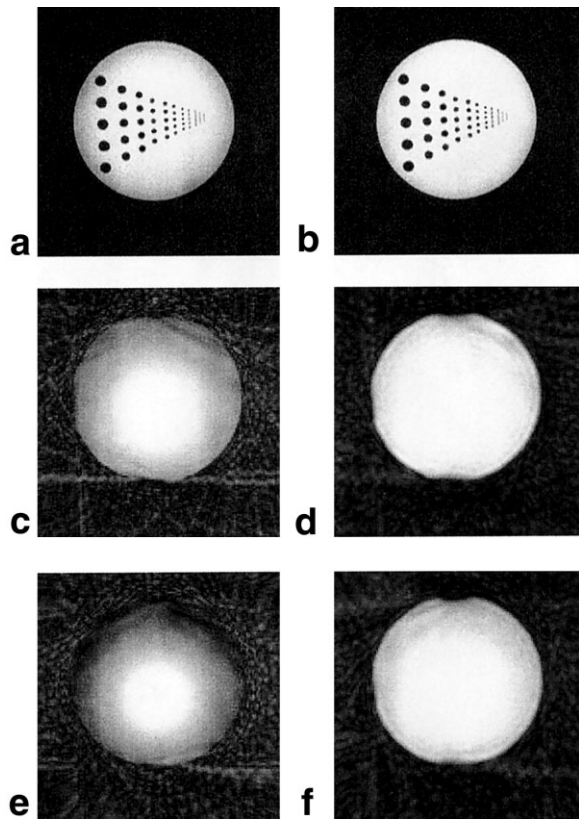
FIG. 5. Images showing, directly, the effects of magnetic field inhomogeneities. Shown is a stock spin warp scout image obtained **(a)** without and **(b)** with a prior MAP shim sequence. The image shows a clear "cupping" artifact with the edge of the phantom having a lower intensity than the center in the unshimmed image. The image intensity across the phantom is uniform after MAP shim. **(c–d)** Images of a 200 mm diameter spherical phantom made with the s1705 sequence. Image **c** was obtained using the parameters given in Table 1. Image **d** was obtained using half the gradient strength (and slew rate) and computed only within a 250 mm field of view. **(e–f)** Images of the spherical phantom made with the s1707 sequence. Image **e** was obtained using the parameters given in Table 1 while image **f** was obtained using half the gradient strength. Images **c–f** may be compared with images **a–f** in Figure 3.

arise from sensitivity to magnetic field inhomogeneities. The cupping artifact is removed from the scout images through the application of the MAP shim sequence. The MAP shim does not remove the cupping artifact from the STAR images; however, no STAR reconstruction is possible if the MAP shim is not applied. The implication seems to be that the cupping would be removed from the STAR images if the field could be further shimmed. Extreme cupping was observed in images of the spherical phantom. The cupping artifact was removed, at the expense of image resolution, by reducing the gradient amplitudes. At a first look, it appears that the receiver bandwidth is not adequate in the images of Fig. 5c,e. However, calculations (see Table 1) indicate that there is more than enough receiver bandwidth. One possibility is that the stock frequency centering algorithm did not adequately center the received frequency within the receiver bandwidth—this might have happened because of the small value of $1/T$. The streaking

artifact appears to emanate primarily from the air bubble in the spherical phantom, where there is a sharp susceptibility gradient. This artifact may be due to an effect of sharp susceptibility gradients that is different from the signal dropout effect caused by reduced $T_2^*$. For example, near the air–water meniscus in the phantom there is a large background magnetic field gradient in the direction across the air–water interface. The background gradient would "shift" the gradient echo signal out of the acquisition window when the readout gradient is perpendicular to the air–water interface but not when the gradient is aligned with the air–water interface. This effective modulation of signal with readout angle could be the cause of the streaking artifact in regions where there are large susceptibility gradients. Future measurements of field inhomogeneities may help to resolve these apparent problems with susceptibility/inhomogeneity caused reconstruction artifacts.

Increasing the circular part of the STAR trajectory by increasing the angle $\alpha$ leads to $k$-space trajectories that cross each other away from the origin (see Fig. 2c). Sequences, such as large $\alpha$ STAR or rosettes, that employ crossing trajectories are known to have a chemical shift selectivity (11,19). The images obtained in this study indicate, however, indicate that such large $\alpha$ STAR sequences will be more sensitive to magnetic field inhomogeneities, in spite of reduced gradient slew rate requirements. Based on these observations, it would appear to follow that sequences, such as the rosette, that are completely curvilinear should have considerably more sensitivity to magnetic field inhomogeneities than STAR or purely radial sequences. However, it is the author's experience that spiral sequences, which are completely curvilinear, are less sensitive to magnetic field inhomogeneities than the STAR trajectory.

The image contrast in STAR images will be different from conventional spin warp style radially acquired images because of the multiple passes through the origin of $k$-space. With the gradient echo sequence used in this study, contrast depended more heavily on the number of interleaves than on the number of petals per interleaf. Such contrast dependence was probably due to the different quasi-steady state reached in the course of the acquisition due the the application of the 40° flip angle, $T_R = 100$ ms repetition with each interleaf.

In addition to cine acquisition and heart imaging, where the radial nature of the STAR trajectory has been shown here to be robust to motion artifact, there are other potentially useful applications for the STAR method, once the sources of the artifacts identified in this work are eliminated. One is the imaging of moving objects similar to the PROPELLER method (8). For each individual STAR acquisition, it is possible to reconstruct a low-resolution image. The low-resolution images may then be aligned to each other and the measured translations and rotations used to compensate for the motion in the high-resolution image reconstruction. Another application is to use sliding window reconstruction in a continuously repeating interleaf acquisition. With the sliding window, acquisitions 1 to $B$ would be used to reconstruct the first image, acquisitions 2 to $B + 1$ would be used to reconstruct the second image, etc. Sliding window reconstruction, combined with a

PROPELLER-like realignment scheme, could be a useful cine imaging method.

## CONCLUSION

Through the simple expedient of increasing the angular sampling rate, the apparent sensitivity of the radial STAR imaging method to magnetic field inhomogeneities may be overcome. The ability to acquire multiple radial lines in one acquisition allows one the freedom to increase angular sampling rates without a significant penalty in acquisition time. The resulting apparent reduced sensitivity to magnetic field inhomogeneities then may make it possible to realize the inherent motion robustness of radial imaging. Applications may be anticipated for the STAR method in fast chemical shift imaging and in the high-resolution imaging of moving objects in real time.

## ACKNOWLEDGMENTS

## REFERENCES

1. Glover GH, Pauly JM. Projection reconstruction techniques for the reduction of motion effects in MRI. Magn Reson Med 1992;28:275−289.
2. Glover GH, Lee AT. Motion artifacts in fMRI: comparison of 2DFT with PR and spiral scan methods. Magn Reson Med 1995;33:624−635.
3. Junga KJ, Cho ZH. Reduction of flow artifacts in NMR diffusion imaging using new angle tilted line-integral projection reconstruction. Magn Reson Med 1991;19:349−360.
4. Gmitro AF, Alexander AL. Use of a projection reconstruction method to decrease motion sensitivity in diffusion-weighted MRI. Magn Reson Med 1993;29:835−838.
5. Nishimura DG, Jackson JI, Pauly JM. On the nature and reduction of the displacement artifact in flow images. Magn Reson Med 1991;22:481−491.
6. Jackson JI, Nishimura DG, Macovski A. Twisting radial lines with application to robust magnetic resonance imaging of irregular flow. Magn Reson Med 1992;25:128−139.
7. Pipe JG. An optimized center-out k-space trajectory for multishot MRI: comparison with spiral and projection reconstruction. Magn Reson Med 1999;42:714−720.
8. Pipe JG. Motion correction with PROPELLER MRI: application to head motion and free-breathing cardiac imaging. Magn Reson Med 1999;42: 963−969.
9. Ahn CB, Kim JH, Cho ZH. High-speed spiral-scan echo planar NMR imaging-I. IEEE Trans Med Imag 1986;5:2−7.
10. Meyer CH, Hu BS, Nishimura DG, Macovski A. Fast spiral coronary artery imaging. Magn Reson Med 1992;28:202−213.
11. Noll DC. Multi-shot rosette trajectories for spectrally selective MR imaging. IEEE Trans Med Imag 1997;16:372−377.
12. Noll DC. Simultaneous multislice acquisition using rosette trajectories (SMART): a new imaging method for functional MRI. Magn Reson Med 1998;39:709−716.
13. Sarty GE. Critical sampling in ROSE scanning. Magn Reson Med 2000; 44:129−136.
14. Silva AC, Barbier EL, Lowe IJ, Koretsky AP. Radial echo-planar imaging. J Magn Reson 1998;135:242−247.
15. Sarty GE. Reconstruction of nuclear magnetic resonance imaging data from non- Cartesian grids. In: Hawkes P, editor. Advances in imaging and electron physics, vol. 111. New York: Academic Press; 1999. p 243−236.
16. Sarty GE. The natural k-plane coordinate reconstruction method for magnetic resonance imaging: mathematical foundations. Int J Imag Syst Tech 1997;8:519−528.
17. Sarty GE, Bennett R, Cox R. Direct reconstruction of non-Cartesian k-space data using a non-uniform fast Fourier transform. Magn Reson Med 2001;45:908−915.
18. Shankaranarayanan A, Simonetti OP, Laub G, Lewin JS, Duerk JL. Real time and segmented true FISP cardiac cine MRI using radial trajectories. ISMRM Workshop on Minimum MR Data Acquisition Methods: making more with less. Marco Island, Florida, 20−21 October, 2001.
19. Scheffler K, Henning J. Frequency resolved single-shot MR imaging using stochastic k-space trajectories. Magn Reson Med 1996;35:569−576.